Micronization as a solution for enhancing the thermal insulation of nanocellular poly(methyl-methacrylate) (PMMA)

Ismael Sánchez-Calderón [a],[*], Victoria Bernardo [b], Daniel Cuadra-Rodríguez [a], Judith Martín-de-León [a], Miguel Ángel Rodríguez-Pérez [a],[c]

[a] *CellMat Laboratory. Campus Miguel Delibes. Faculty of Science. Condensed Matter Physics Department. University of Valladolid, Paseo de Belén 7, 47011, Valladolid, Spain*
[b] *CellMat Technologies S.L., Paseo de Belén 9-A, 47011, Valladolid, Spain*
[c] *BioEcoUVA Research Institute on Bioeconomy, University of Valladolid, 47011, Valladolid, Spain*

ARTICLE INFO

ABSTRACT

This work shows a route to reduce the thermal conductivity of nanocellular poly(methyl-methacrylate) (PMMA). This approach is based on micronizing to replace the continuous solid phase by a discontinuous one. PMMA powders with densities of 147–195 kg/m^3, formed by particles of 100 μm with nanometric cells inside them, are produced by milling. Micronization allows increasing the overall porosity maintaining the cell size. Results prove that after milling it is possible to obtain open cell nanoporous PMMA powders with thermal conductivity below that of the bulk materials (15% reduction). The reduction is not only due to a density decrease, but a result of the new structure of the powder material. The discontinuity of the solid phase and the increase in radiation extinction are the key factors allowing this improvement. This route is confirmed as a promising alternative to enhance the performance of nanocellular polymers.

1. Introduction

Nowadays, nanocellular polymers (a new class of materials in the frontier of materials and polymer science characterized by cell sizes below 1 μm) have aroused great interest in the scientific community owing to their unique combination of properties like lightweight, transparency, low thermal conductivity, enhanced mechanical properties in comparison with microcellular polymers and recyclability, among others [1–5]. One of the most relevant features of these systems is their reduced thermal conduction through the gas phase due to the Knudsen effect [6]. Knudsen effect takes place in other nanoporous materials that show extremely low thermal conductivities, such as aerogels or fumed silicas [7–10]. As a consequence, it was claimed several times in the last years that nanocellular polymers could also be potentially used as super thermal insulators (thermal conductivities below that of air, 24.4 mW/(m·K) at 10 °C) [11–13].

However, recent works have shown that the minimum thermal conductivity that can be reached with these materials is much higher than those of other nanoporous materials such as aerogels for instance [14,15]. While there is indeed a reduction in the gas conduction when

decreasing the cell size to the nanoscale due to the Knudsen effect, as proved by Notario et al. [6], the other two heat transfer mechanisms (radiation and conduction through the solid phase) increase the total thermal conductivity. Regarding the radiation contribution, Bernardo and coworkers [16] proved experimentally a reduction of the scattered radiation in nanocellular polymers. This behavior was also theoretically reported by Wang et al. [14] and Buahom et al. [15]. Both authors developed mathematical models to predict the thermal conductivity of microcellular and nanocellular polymer foams. Those works showed that when the cell size is reduced to the nanoscale the radiation term increases, especially at high expansion ratios (i.e., low relative densities). Finally, in our recent previous work, we developed a semi-empirical model to predict the thermal conductivity of low-density microcellular and nanocellular poly(methyl-methacrylate) (PMMA) [17]. In that work, we proved that radiation is indeed a highly affecting factor when density and cell size decrease. In addition, the conduction through the solid phase, particularly the so-called structural factor (g), dominates the expected thermal conductivity. While minimum values of 34 mW/(m·K) were predicted at 10 °C for the experimentally calculated structural factor ($g = 0.89$), values as low as 22 mW/(m·K) could be

reached if this parameter is reduced, for instance, to $g = 0.3$.

Therefore, in order to enhance the thermal insulation of nanocellular polymers, there are, at least, two possible routes. On the one hand, one possibility is the addition of infrared radiation blockers (IR-blockers) to the polymer matrix to reduce the radiation contribution [18,19]. However, the addition of IR-blockers can modify the foaming process, affecting the cellular structure and even leading to higher densities [20]. The dispersion of the opacifiers in the polymer matrix before foaming is also a challenge because high shears are required during the extrusion process to avoid their agglomeration [20]. In addition, the process becomes more challenging as the percentage of IR-Blocker on the polymer matrix increases. On the other hand, the alternative approach is to reduce the thermal conductivity through the solid phase by modifying the solid cellular structure. This paper is focused on the latter strategy, particularly in the production of micronized nanocellular powders (Fig. 1). By means of micronization, it is possible to transform a continuous solid phase in the cellular structure into a discontinuous solid phase with the nanocells inside the micrometric particles. The micronized system is now characterized by a double porosity formed by nanometric cells (inside the particles) and micrometric voids (among the particles). In this sense, micronized nanocellular powders may look similar to foams with a double population of cells (bimodal structures characterized by micrometric and nanometric cells) [21–24]. Bernardo et al. [21] studied and modeled the thermal conductivity of bimodal structures. They showed that the micrometric cells help to decrease the density of the foam, whereas the nanocellular cells decrease the thermal conductivity due to the Knudsen effect. Both factors decrease the overall thermal conductivity. Gong and coworkers [22] developed a model for bimodal cellular structures, observing too that the presence of large cells helps to reduce the density and maximize the expansion, thus decreasing thermal conduction. Then, micronization is expected to reduce density and help in reducing the conduction mechanism. However, in the micronized nanocellular powders, the solid cellular structure is discontinuous, whereas in foams with bimodal structures the solid phase is continuous. This is a key difference that can lead to additional improvements in the micronized material. This discontinuous type of structure is similar to that of advanced thermal insulators, such as aerogels or fumed silica. In those systems, formed by numerous nanometric particles, the contact points between the particles act as additional thermal resistances, sharply reducing thermal conductivity through the solid phase [8,25]. For aerogels, Lu et al. [26] proved that the conduction through the solid phase can be as low as 6 mW/(m·K) (at 27 °C) for aerogels of density 180 kg/m³. In the case of fumed silica, values of 3 mW/(m·K) (at 21 °C) are found for the same densities (180 kg/m³) [10]. These low values correspond to structural factors g as low as 0.05 [27, 28], 18 times lower than that calculated for nanocellular PMMA sheets. As a comparison, note that in a nanocellular PMMA sample of 180 kg/m³ the conduction through the solid phase was found to be 24 mW/(m·K) (at 10 °C). This extreme change is due to the discontinuity of the structure in aerogels and the continuity of this structure in nanocellular

polymers. Moreover, the transition from a continuous nanocellular polymer to a micronized material could lead to other advantages, such as a density reduction since the powder particles would be surrounded by air. Also, the presence of micrometric voids between the powder particles could act as scattering points for infrared radiation, reducing the radiation contribution [15]. Furthermore, the addition of IR-blockers would be easier in the micronized material because the powdered IR-blocker could be directly blended with the micronized material. This approach was successfully used in many works of silica particles where powdered opacifiers are added, obtaining good distributions and good thermal conductivity reductions [10,29–31]. As commented before, dispersion is more challenging in the solid and the amount of IR-blockers is limited to allow proper foaming. Finally, another possible further advantage is that the production of micronized nanocellular polymers would be easier to scale-up.

In the present work, micronized nanocellular PMMA powders are produced by milling nanocellular PMMA foamed samples with densities ranging 150–220 kg/m³ and cell sizes of 400 nm. The obtained powders are characterized through several techniques to determine the apparent density, the open cell content, and the particle size. Finally, the thermal conductivity is measured using a heat flow meter (steady-state method) and compared to the bulk foamed samples to analyze the effect of the micronization on the different heat transfer mechanisms.

2. Experimental

2.1. Materials and sample preparation

Three nanocellular materials based on PMMA were produced by gas dissolution foaming. The PMMA grade used was PLEXIGLAS® 7H kindly supplied by Röhm GmbH. This PMMA presents a density of 1190 kg/m³, a melt flow index of 0.77 g/10 min (measured at 230 °C and 2.16 kg), and a glass transition temperature of 110.4 °C measured by DSC (model DSC3+, Mettler). Details of the procedure to produce and characterize these samples can be found in our previous work [17]. The main features of these nanocellular samples (density (ρ), cell size in three dimensions (φ_{3D}), normalized standard deviation of the cell size distribution (SD/φ_{3D}), open cell content (OC), and thermal conductivity (λ) at 10 °C are collected in Table 1. Samples are named based on their density (lowest density (LD), medium density (MD), and highest density (HD)), which ranges between 150 and 220 kg/m³. The samples are nanocellular (cell size between 394 and 468 nm) with a homogeneous cellular structure (normalized standard deviation of the cell size lower than 0.5). The open cell content ranges from almost 100% for the LD bulk sample to around 74% for the HD bulk sample. The thermal conductivity ranges between 39 and 44 mW/(m·K) at 10 °C. As expected, the thermal conductivity is observed to increase with increasing the density of the samples.

The bulk nanocellular samples were pre-grinded in a grinding machine (550 W of power) and then micronized using a rotor beater mill SR
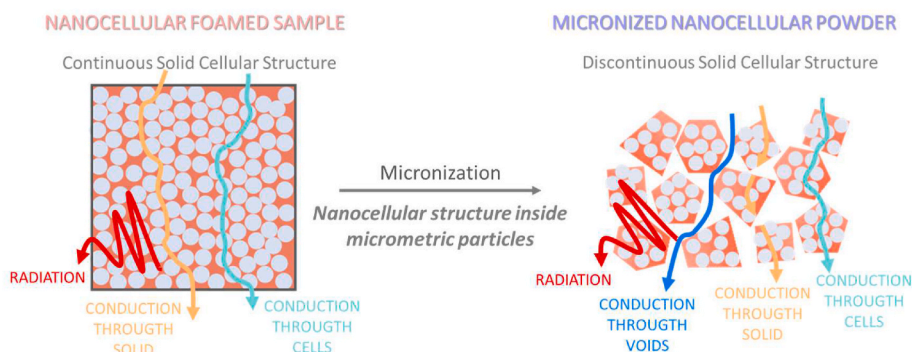

Fig. 1. Main concept of this work: micronization as a possible solution to enhance the thermal insulation of nanocellular polymers.

Table 1

Density, cell size, normalized standard deviation of the cell size, open cell content, and thermal conductivity at 10 °C of the bulk nanocellular samples.

Sample	Bulk Nanocellular Samples					
	ρ (kg/m^3)	ρ_r	φ_{3D} (nm)	SD/φ_{3D}	OC (%)	λ @ 10 °C (mW/(m·K))
LD	154 ± 10	0.13	468	0.47	99 ± 1	39.4
MD	186 ± 9	0.16	408	0.47	86 ± 1	41.7
HD	218 ± 10	0.18	394	0.43	74 ± 1	44.0

300 (Retsch). For both processes, the samples were immersed in liquid nitrogen for at least 5 min to brittle them and to preserve the cellular structure during milling. Grinding time was 15 s. The objective of the pre-grinding is to obtain particles smaller than $5 \times 5 \times 5$ mm^3 able to be dosed in the rotor beater mill. The rotor beater mill speed was set at 10000 rpm, and the cold material was dosed each 15 s in small quantities to prevent excessive heating of the system. The sieve used to micronize the samples after impact was a trapezoid stainless sieve with holes of 350 µm size. Note that the micronization is almost instantaneous and that the particle size is controlled by the size of the trapezoid holes of the sieve used. The sieve determines the maximum size of the powder particles but the friction during the rotation together with the cryogenic cooling may result in smaller particles as seen later. The processing conditions were optimized to prevent the collapse of the foam structure. After the milling process, the resultant materials were homogeneous powders with micrometric particles. These micronized samples were characterized using the following techniques.

2.2. Characterization of the micronized nanocellular polymers

2.2.1. Density

The apparent density (ρ_{app}) of the micronized samples was obtained according to ISO 60 [32]. The ratio between the density of the bulk nanocellular polymer before milling (ρ) and the apparent density of the powder have been defined as the packing factor ($F_{density} = \rho_{app}/\rho$). Therefore, the packing factor is the volume fraction occupied by the nanocellular polymer particles regarding the total volume of the powder assuming that each particle in the powder has the same density as the original bulk material, that is, there is not an increase in density after the milling process. See Supporting **Information Section S1** for more information about the parameters describing the powder.

2.2.2. Surface morphology (SEM)

A Scanning Electron Microscope (FlexSEM 1000 VP-SEM) was used to visualize the surface of the micrometric particles and evaluate the effect of the micronization process.

2.2.3. Open cell content

Open cell content (*OC*) of the micronized samples was obtained through Equation (1), using a gas pycnometer (model AccuPyc II 1340, Micromeritics). The gas used was N$_2$.

$$OC\ (\%) = \frac{V - V_{pyc}}{V(1 - \rho_r)} \cdot 100 \tag{1}$$

Where *V* is the geometric volume and V_{pyc} is the volume obtained from the pycnometric measurement. *V* is calculated after dividing the weight of the total amount of powder particles introduced in the pycnometer between the density of the powder particles. The open cell was calculated twice. In the first calculation, *OC* was calculated assuming that the density of the particles is the same as the density of the bulk nanocellular polymer (non-corrected value). Then, this value was corrected (OC_{corr}) after calculating the real density of the powder particles using

tomography (see next section).

2.2.4. Packaging: porosity, number particle size, and number void size (X-ray tomography)

The powder packaging was studied using a laboratory X-ray tomography set-up [33–35]. The set-up consists of an X-ray microfocus source (Hamamatsu) with a maximum output power of 20 W (spot size: 5 µm, voltage: 20–100 kV, current: 0–200 µA). Emitted X-rays form a cone beam of 39°, allowing up to obtain 20 times magnification in the experiments. The transmitted X-ray intensity is collected with a high-sensitivity flat panel connected to a frame grabber (Dalsa-Coreco), which records the projected images. The detector is composed of a matrix of 2240×2344 pixels, each with a size of 50 µm.

A Kapton cylinder of around 5 mm of diameter and 10 mm in height was used to hold the powder. Kapton is transparent to the X-ray radiation allowing the acquisition of images of the powder inside the cylinder. The linear stage was placed in a position so that the pixel size was 3 µm. The tube voltage, current, exposure time, and rotation step were set to 55 kV, 170 µA, 1 s, and 0.3°. To enhance the contrast in the reconstructed images, each projection was the result of integrating three consecutive images. Once all the projections were acquired, the reconstruction process of the tomogram was carried out using the Octopus server/client reconstruction package [36] by reconstructing 1800 slices (equivalent to 5.4 mm in height). Due to the spatial resolution of the tomographic system (3 µm), the reconstructed slices (Fig. 2a) can be used to analyze the volume occupied by the powder particles and the voids with respect to the total volume. With this aim, the slices were binarized using the software ImageJ/FIJI (Fig. 2b). Once binarized, the particles are characterized by white pixels, whereas the voids pixels are black. Therefore, the number of white pixels regarding the total is the volume fraction of foamed particles, or in other words, the packaging factor. To distinguish this value from the one calculated with the density ($F_{density}$), the packaging factor calculated with tomography is referred as F_T. Note that this packaging factor is the real fraction of foamed particles since it is directly measured in the powdered material. From this value, it is possible to calculate the real particle density ($\rho_{particle}$) of the powder particles as $\rho_{particle} = \rho_{app}/F_T$.

Meanwhile, the void volume fraction obtained through X-ray tomography ($X_{v,T}$) is calculated as the number of black pixels regarding the total. Note that the overall porosity (that is, the overall gas volume fraction) of the material is the sum of the cell volume fraction and the void volume fraction (see details about these parameters in Supporting **Information Section S1**).

Furthermore, the local thickness analysis ImageJ/FIJI tool was used to study the powder particle size distribution (Fig. 2c) and the void size distribution (Fig. 2d). The void size is the size of the air regions that appear between the powder particles (see Supporting **Information Fig. S2).** By definition, the local thickness is the diameter of the largest sphere that fits inside the object and contains the point. Thus, this tool associates a thickness value (represented by a determined color) to each pixel. Hence, each pixel is characterized by a color that is related to a distance. From the obtained results the distribution in percentage of number (%number) of either the particle size **(Fig. 2e)** or the void size **(Fig. 2f)** can be obtained. Also, it is possible to calculate the average particle size (D_T) and the average void size (V_T). The mean number particle/void size is obtained by performing the arithmetic mean as commented in Supplementary Information S2 **Equation S(8)** [37]**.** Note that this technique assumes spherical particles.

2.2.5. Number particle size (Image analysis using autocell)

In this work, image analysis is used to characterize the particle size distribution using the software Autocell **(Fig. 3).** Autocell is an image analysis tool developed by CellMat Technologies S.L. (Valladolid, Spain) to characterize the cellular structure of different types of foamed samples (details about it can be found in [38]). First, the powder is dispersed on a contrasting background to take a picture with a small portable
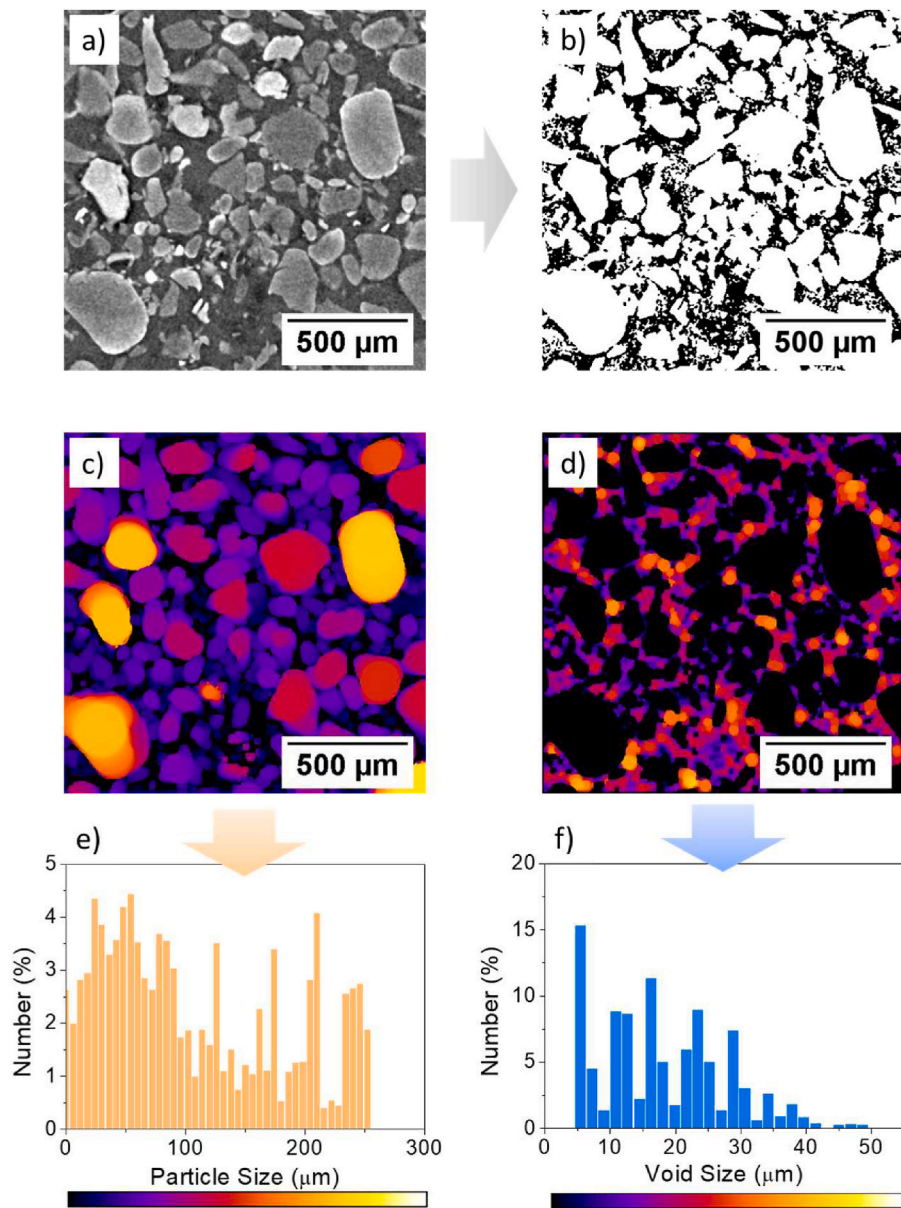
Fig. 2. a) Raw X-ray tomography slice, b) binarized X-ray tomography slice (in white the powder particles and in black the voids), c) powder particles local thickness map slice, d) voids local thickness map slice, e) particle size distribution, and f) void size distribution.
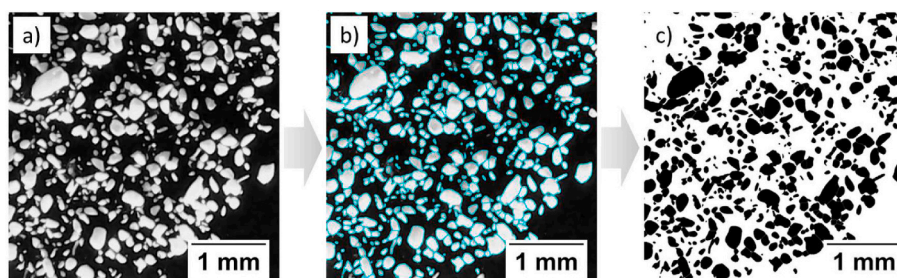

Fig. 3. Methodology for calculating the number particle size using image analysis and the software Autocell: a) raw image, b) selection of particles on the raw image, and c) mask to be analyzed.

benchtop optical microscope (**Fig. 3a**). This setup allows measuring accurately particles larger than 15 μm. Then, the image is analyzed with Autocell. The software selects the powder particles (**Fig. 3b**) and creates a mask (**Fig. 3c**) which is used to obtain the particle size distribution.

More than 800 particles were analyzed. This technique assumes spherical particles and gives the powder particles size distribution in percentage of number (%number), from which it is possible to calculate the average particle size (D_A). The mean number particle size is obtained by

performing the arithmetic mean as commented in **Supplementary Information S2 Equation S(9)** [37].

2.2.6. Volume particle size (dynamic laser diffraction)

Dynamic laser diffraction measurements were performed to study the particle size distribution. Experiments were carried out at CENIEH (Burgos, Spain) using a LS13 320 Particle Size Analyzer (Beckman Coulter). The powder particles are dispersed for 1 min in ethanol with ultrasounds. Then, they are analyzed in the ULM module. This technique assumes spherical particles and provides the particle size distribution in percentage of volume (%volume), from which it is possible to calculate the average particle size (D_{DLS}). Note that in volume distributions, the larger particles have a higher weight than the smaller ones. The mean volume particle size, also known as De Brouckere's mean diameter, is provided by the analysis software, and it is obtained as commented in **Supplementary Information S2 Equation S(10)**. [37,39]. Dynamic laser diffraction allows measuring particles between 40 nm and 2000 μm. Note that the particle size was also calculated with tomography (D_T) and image analysis (D_A): the three techniques are later compared.

2.2.7. Thermal conductivity measurements (Heat flow meter)

Thermal conductivity measurements were performed using a thermal heat flow meter model FOX 200 (TA Instruments/LaserComp, Inc.), which measures according to ASTM C518 and ISO 8301 [40,41]. Measurements were performed in steady-state conditions. For the measurements, the powder was placed between the two plates, promoting a temperature gradient through the material thickness. A polyurethane foam mask (with a size of $200 \times 200 \times 14$ mm^3) with a hole of 120×120 mm^2 in the center was used to hold the free powder. An aluminum foil placed on the bottom of the mask was used to avoid the loss of powder. The measurements were performed at 10, 20, 30, and 40 °C. The temperature gradient (ΔT) was set to 20 °C in every case (i.e., for the measurement at 10 °C, the temperature goes from 0 °C in the upper isothermal plate to 20 °C in the lower one). Note that the active area of

solid PMMA. The conductivity of the solid PMMA depends on the temperature as shown in Equation (3) [17]. Meanwhile, the *g* factor of the micronized material is an unknown factor that can be calculated from the experimental results, as will be explained later. The *g* factor is related to the solid structure tortuosity, and it is known to be much lower than 1 in low-density conventional foams [42]. For nanocellular polymers, a high value of around 0.9 was calculated in a previous work [17]. Then, understanding the *g* factor would be key to determine the effect of micronization in the heat transfer by conduction through the solid material.

$$\lambda_s(mW/(m \cdot K)) = \lambda'_s g X_{s,powder} = (0.2060T + 115.5811)gF\rho_{r,particle} \quad (3)$$

Secondly, in this system, due to the presence of cells and voids, conduction through the gas phase must be divided into two parts (Equation (4)). The conduction through the gas phase (λ_g) depends on the gas volume fraction and the thermal conductivity of the gas. On the one hand, the voids volume fraction ($X_{g,voids}$) corresponds to the volume fraction not occupied by the powder particles, which is $1 - F$ (Supporting **Information Section S1**). For this phase, the conductivity of the gas in the voids ($\lambda'_{g,voids}$) is that of the air, which depends on temperature as seen in Equation (4). [43]. On the other hand, the cells volume fraction ($X_{g,cells}$) can be calculated as $F(1 - \rho_{r,particle})$ (Supporting **Information Section S1**). In this case, the conductivity of the gas inside the nanometric cells ($\lambda'_{g,cells}$) is not that of the air, but it is reduced due to the Knudsen effect. This effect implies that when cell size is comparable to or smaller than the mean free path of the gas molecules they collide more often with the cell walls than among them, reducing the energy transfer [9]. Therefore, the conductivity of the gas inside the cells is reduced. Thus, the conduction through the cells phase also depends on the conductivity of air (which is function of the temperature), the cell size (φ), an intrinsic parameter that considers the transfer of energy between the gas molecules and the solid structure (β), the temperature (T), the pressure (p), the molecule diameter (d_m), the ideal gas constant (R) and the Avogadro's number (N_A).

$$\lambda_g(mW/(m \cdot K)) = \lambda_{g,cells} + \lambda_{g,voids} = \lambda'_{g,cells} X_{g,cells} + \lambda'_{g,voids} X_{g,voids} = \frac{(0.07411T + 3.40294)F(1 - \rho_{r,particle})}{1 + \frac{2\beta}{\varphi}\frac{RT}{\sqrt{2}\pi d_m^2 N_A p}} + (0.07411T + 3.40294)\cdot(1 - F) \quad (4)$$

the FOX 200 heat flux transducers is 75×75 mm^2. Therefore, the samples have larger dimensions than the heat flux transducers (120×120 mm^2 vs 75×75 mm^2). Then, the polyurethane mask does not affect the measured thermal conductivity since it is not in contact with the heat flux transducers. The absolute thermal conductivity deviation error for this device is 2%.

3. Thermal conductivity modeling

The total thermal conductivity (λ_t) can be described as the sum of three contributions: conduction through the solid phase (λ_s), conduction through the gas phase (λ_g), and thermal radiation (λ_r), as shown in Equation (2).

$$\lambda_t = \lambda_s + \lambda_g + \lambda_r \quad (2)$$

First, conduction through the solid phase (λ_s) depends on the solid volume fraction (X_s), the conductivity of the solid matrix (λ'_s), and a structural factor *g* (Equation (3)). For the powder materials, the solid volume fraction ($X_{s,powder}$) can be calculated as the product between the packing factor *F* (in this work, obtained from tomography) and the relative density of the powder particles (Supporting **Information Section S1**). The relative density of the particle is defined as $\rho_{r,particle} = \rho_{particle}/\rho_s$, where $\rho_{particle}$ is the particle density and ρ_s is the density of the

Finally, thermal radiation (λ_r) depends on the temperature (T), the Stefan-Boltzmann constant (σ), the refractive index (n), and the extinction coefficient (K_e) (Equation (5)). The extinction coefficient of the micronized material is an unknown factor that can be calculated from the experimental results, as will be explained later. The extinction coefficient quantifies the amount of radiation that the cellular material can block, either by absorption of the polymer matrix or scattering of the cell structure [15–17], so its determination is critical to understand the radiation heat transfer in the micronized material. The factor ·1000 in Equation (5) is included to obtain the thermal radiation in mW/(m·K).

$$\lambda_r(mW/(m \cdot K)) = \frac{16n^2\sigma T^3}{3K_e}\cdot 1000 \quad (5)$$

Finally, after the mentioned considerations, Equation (2) can be expanded into Equation (6) for the micronized system. A detailed list of the constants, values, and input units used in the calculations of the thermal conductivity can be found in Supporting **Information Section S3**. Note that the input units are on the International System of Units (SI) but the final result of the calculation is in mW/(m·K) due to the low thermal conductivity of the materials.

$$\lambda_t(mW/(m \cdot K)) = (0.2060T + 115.5811)gF\rho_{r,particle} + \frac{(0.07411T + 3.40294)F(1 - \rho_{r,particle})}{1 + \frac{2\beta}{\varphi}\frac{RT}{\sqrt{2}\pi d_m^2 N_A p}} + (0.07411T + 3.40294)\cdot(1 - F) + \frac{16n^2\sigma T^3}{3K_e}\cdot1000 \qquad (6)$$

In this work, the solid structural factor *g* and the extinction coefficient K_e are going to be obtained following the methodology developed in our previous work [17]. The method consists of subtracting the solid and gas thermal contributions (as both contributions depend on the temperature) to calculate the *g* factor, which is obtained by iteration using the condition that the thermal conductivity must be 0 mW/(m·K) at 0 K. Once the *g* is obtained, K_e can be easily extracted from the slope of the curve λ-T^3 as proposed by Almeida et al. [19]. Fig. 8 summarizes the results of this study in comparison to the data obtained previously for the bulk materials.

4. Results and discussion

4.1. Effect of micronization on the density and cellular structure

Table 2 summarizes the apparent density, packing factor, and open cell content of the three micronized powders obtained through the density and X-ray tomography measurements. Regarding the density measurement, it is observed that after micronization, the density is reduced compared to that of the bulk material (Table 1) due to the presence of voids (air) between the powder particles. For instance, for sample LD the density reduces from 154 to 147 kg/m^3. On the one hand, the packing factor obtained through the density measurement ($F_{density}$) is around 0.94 (which would mean a density reduction of 6%). Taking into account the deviation of these measurements, we can claim that the three samples show almost the same packing factor. However, this $F_{density}$ value is quite high: for random packaging of non-spherical particles, packaging factors as high as 0.77 are expected [44,45]. Therefore, the hypothesis used to calculate $F_{density}$ that the powder particles have not suffered densification could be incorrect. To prove this fact, X-ray tomography measurements were performed. Fig. 4 shows the tomography reconstructions of the three samples. From the reconstructed slides, the volume occupied by the powder particles with respect to the total volume has been calculated, that is, the packaging factor (F_T) (Table 2). The packing factor obtained through tomography is around 0.76, matching with the literature results as commented previously [44,45]. It is observed that the packing factors calculated from tomography are about 22% lower than those obtained from the apparent density measurement. Then, it is confirmed that the hypothesis used to calculate $F_{density}$ was incorrect and the materials suffered an increase in density during the milling process. The density of the particles is higher than that of the bulk materials (around 22% higher on average) (Tables 1 and 2). The increase in density can be due to the forces involved in the milling process, that is, the material can be partially compressed and thus densified. However, the densification did not result in noticeable changes in the cellular structure, as it will be seen in Fig. 5. Regarding differences among the three materials, similar packaging factors are obtained regardless the density of the initial bulk sample, meaning same densification level. Thus, the milling process leads to the same result for the three materials. Recall that the micronization is almost instantaneous and that the particle size is controlled by the size of the trapezoid holes of the sieve used.

Regarding the open cell content (Table 2) it increases to more than 90% in all the micronized samples, meaning greater access to the inner cellular structure. Corrected open cell values (obtained from the X-ray tomography measurement) are slightly lower than the non-corrected values (obtained through the density measurement). In addition, Table 2 also includes the void fraction obtained by tomography ($X_{v,T}$) (calculated as $1 - F_T$), which ranges between 20 and 30% in all the materials.

Finally, the cellular structure is preserved after micronization as seen in the example of Fig. 5, where SEM micrographs at different magnifications of the MD bulk (Fig. 4a) and micronized (Fig. 4b) samples are compared. In the micronized material, the cellular structure is visible on the surface of the particles. This explains the increase in the open cell content observed after the milling process. SEM images of the rest of the micronized materials can be found in Supporting **Information Section S4**. The particles present a polyhedral shape as seen in Fig. 4b.

4.2. Particle and void size analysis

The definition and a schematic view of the particle size and void size can be found in Supporting **Information Section S1**. Results of the mean powder particle size (*D*) and the normalized standard deviation of the measurements (*SD/D*) calculated with different techniques (dynamic laser diffraction (D_{DLS}), image analysis (D_A), and tomography (D_T)) are presented in Table 3. Different particle size distribution results (Fig. 6) are obtained with the different techniques used (dynamic laser diffraction, image analysis, or X-ray tomography). Note that dynamic laser diffraction gives the results in volume fraction, whereas image analysis and X-ray tomography provide results in number fraction. In the volume fraction distribution, the larger particles have a higher weight than the smaller ones. Meanwhile, in the number distributions, the number of particles of a given size has a more significant effect than their size. For this reason, the results of dynamic laser diffraction are always higher than those obtained with the other techniques. However, similar trends are observed for the three techniques: the MD sample presents the largest particle size, while the LD shows the smallest. It is also observed that the particle size distribution is wide (Fig. 6), since the normalized standard deviation is usually higher than 0.5 in all cases. Regarding image analysis and X-ray tomography, the two techniques provide similar results, with differences below 25 μm. The lower values obtained with tomography can be due to a better resolution of this technique for low particle sizes. This result supports the use of image analysis as a fast and easy alternative to precisely calculate the particle size with almost

Table 2
Apparent density, relative apparent density, packing factor, and non-corrected open cell content of the powders of the micronized samples obtained through the density characterization. Values of the packing factor calculated by X-ray tomography, void fraction, powder particles density, and corrected open cell considering densification of the particles.

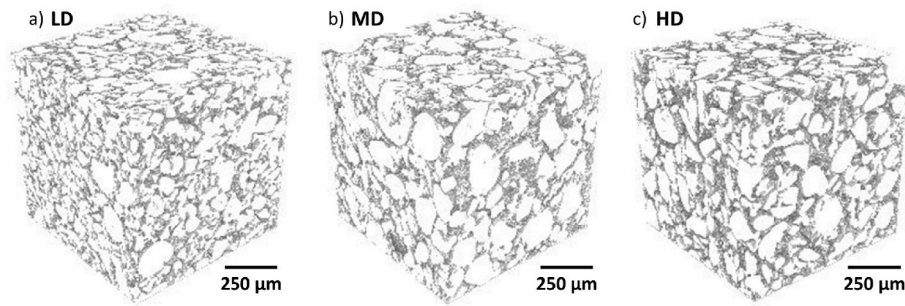| Sample	Density				X-ray Tomography			
	ρ_{app} (kg/m^3)	$\rho_{r,app}$	$F_{density}$	OC (%)	F_T	$X_{v,T}$	$\rho_{particle}$ (kg/m^3)	OC_{corr} (%)
LD	147 ± 2	0.12	0.96 ± 0.08	99 ± 1	0.77 ± 0.09	0.23 ± 0.09	190	98 ± 1
MD	179 ± 3	0.15	0.96 ± 0.06	94 ± 1	0.79 ± 0.05	0.21 ± 0.05	226	92 ± 1
HD	195 ± 3	0.16	0.89 ± 0.05	97 ± 1	0.71 ± 0.07	0.29 ± 0.07	274	97 ± 1

Fig. 4. X-ray tomography reconstruction of a) LD, b) MD, and c) HD micronized nanocellular samples.
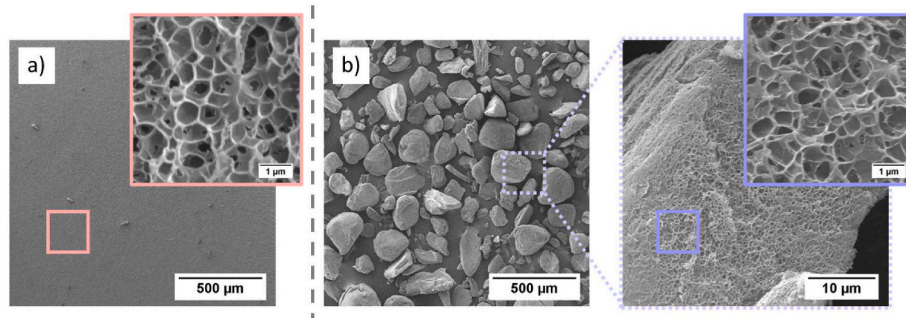

Fig. 5. Example of the effect of micronization on the cellular structure (sample MD): SEM micrographs at different magnifications of a) the inner cellular structure of the bulk sample, and b) the particles and the surface of micronized material.

Table 3
Mean particle size and normalized standard deviation of the particle size distribution calculated with dynamic laser diffraction, image analysis, and X-ray tomography. Mean void size and normalized standard deviation of the void size distribution obtained through X-ray tomography.

Sample	Particle Size						Void Size	
	Dynamic Laser Diffraction (% Volume)		Image Analysis (%Number)		X-ray Tomography (%Number)		X-ray Tomography (%Number)	
	D_{DLS} (µm)	$SD/$ D_{DLS}	D_A (µm)	$SD/$ D_A	D_T (µm)	$SD/$ D_T	V_T (µm)	$SD/$ V_T
LD	157	0.63	94	0.62	69	0.60	25	0.46
MD	229	0.49	102	0.64	110	0.68	19	0.51
HD	178	0.58	100	0.69	86	0.62	26	0.53

the same accuracy as X-Ray tomography.

Table 3 also includes the mean void size (V_T) and normalized standard deviation (SD/V_T) calculated from the X-ray tomography. The average void size is in the range of 20–30 µm (see the distributions of the void size in Supporting **Information Section S5**). Similar values are obtained for the three materials (note that the error associated with the tomography measurements is 3 µm).

4.3. Analysis of the thermal conductivity

Regarding the thermal conductivity of the micronized nanocellular samples, the results obtained at the different temperatures are presented in Fig. 7. Also, the thermal conductivities of the bulk samples have been included in Fig. 7 for the sake of comparison. It is observed that in all cases the micronization process leads to a reduction (about 15%) of the thermal conductivity. For instance, at 10 °C, the thermal conductivity of the HD powder is reduced 7.5 mW/(m·K) with respect to the bulk sample (36.5 vs 44.0 mW/(m·K)). The minimum thermal conductivity is obtained at 10 °C: 33.6 mW/(m·K) for the LD micronized powder. These

results support that the micronization process is a way to reduce the thermal conductivity in nanocellular polymers.

Initially, thermal conductivity reductions could be easily attributed to the lower density and the presence of voids between the powder particles since the conduction through the solid phase decreases (lower solid fraction) and the air have lower thermal conductivity than the nanocellular sample (Equation (6)). However, when the different mechanisms are quantified more interesting results are obtained. In the following paragraphs, the thermal conductivity mechanisms will be analyzed to understand the effect of micronization on thermal conductivity.

On the one hand, it is observed that micronization reduces about 29% the solid structural factor (Fig. 8a). Is important to remark that the solid structure factor is related to the solid structure connectivity which determines the phonon diffusion throughout the material [8,17,42]. As shown in Equation (3), the lower the solid structural factor (*g*) the better to reduce the conduction through the solid phase. Therefore, this reduction could be associated with the transition from a continuous cellular structure (bulk sample) to a discontinuous structure (powder) where the contact points between the particles act as additional thermal resistances (aerogel-like structure) [8,25]. For example, the solid structural factor of the MD sample decreases from 0.89 (bulk) to 0.64 (powder). Therefore, the decrease of the conduction through the solid phase is not only due to the lower relative density but also to the reduction of the solid structure factor. These results once again confirm the initial hypothesis of this work: the generation of a micronized nanocellular polymer reduces conductivity by means of a reduction of the conduction through the solid phase.

On the other hand, the extinction coefficient increases after micronization (Fig. 8b). Note that the extinction coefficient is related to the ability of the material to block (thought absorption or scatter) the radiation. Therefore, the higher the extinction coefficient (K_e) the higher reduction of the radiation contribution (Equation (5)). The extinction coefficient rise is higher as the density of the sample is reduced (27, 18, and 10% for the LD, MD, and HD samples, respectively). For instance,
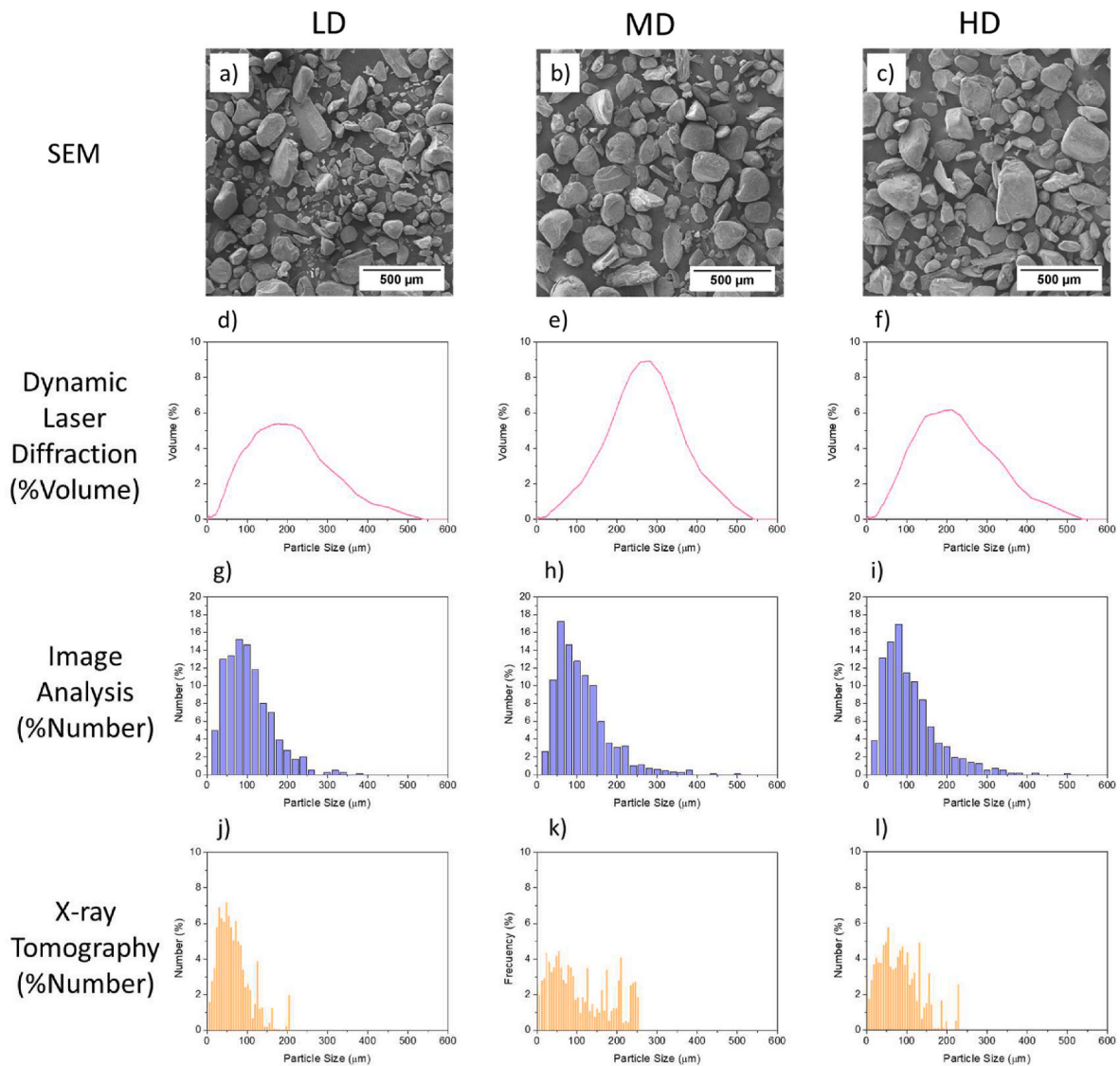
Fig. 6. SEM micrographs (first raw), dynamic laser diffraction %volume particle size distributions (second raw), image analysis %number particle size distributions (third raw), and X-ray tomography %number particle size distributions (fourth raw) of the samples LD (first column), MD (second column) and HD (third column).
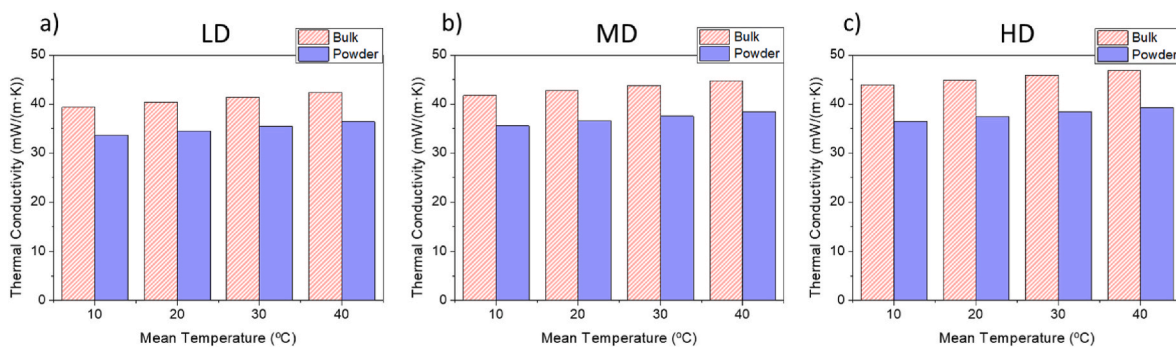

Fig. 7. Experimental thermal conductivities measured at different temperatures of a) LD, b) MD, and c) HD powder.

for the LD sample the extinction coefficient increases from 16.3 cm^{-1} (bulk sample) to 20.6 cm^{-1} (powder). To explain this trend is important to remark that in micronized materials the density is lower, and so is the fraction of solid material available for absorbing infrared radiation. For sake of proper comparison, in Fig. 8c the specific extinction coefficients, which is the extinction coefficient divided by density (bulk or powder

apparent density), are presented. It is observed that the specific extinction coefficient is still higher in the micronized materials than in the bulk samples. For instance, for the LD material the specific extinction coefficient increases from 10.5 to 14.0 m^2/kg. For the materials with higher density the rise in the specific extinction coefficient is about 20%. In nanocellular materials the scattering mechanism changes from Mie to
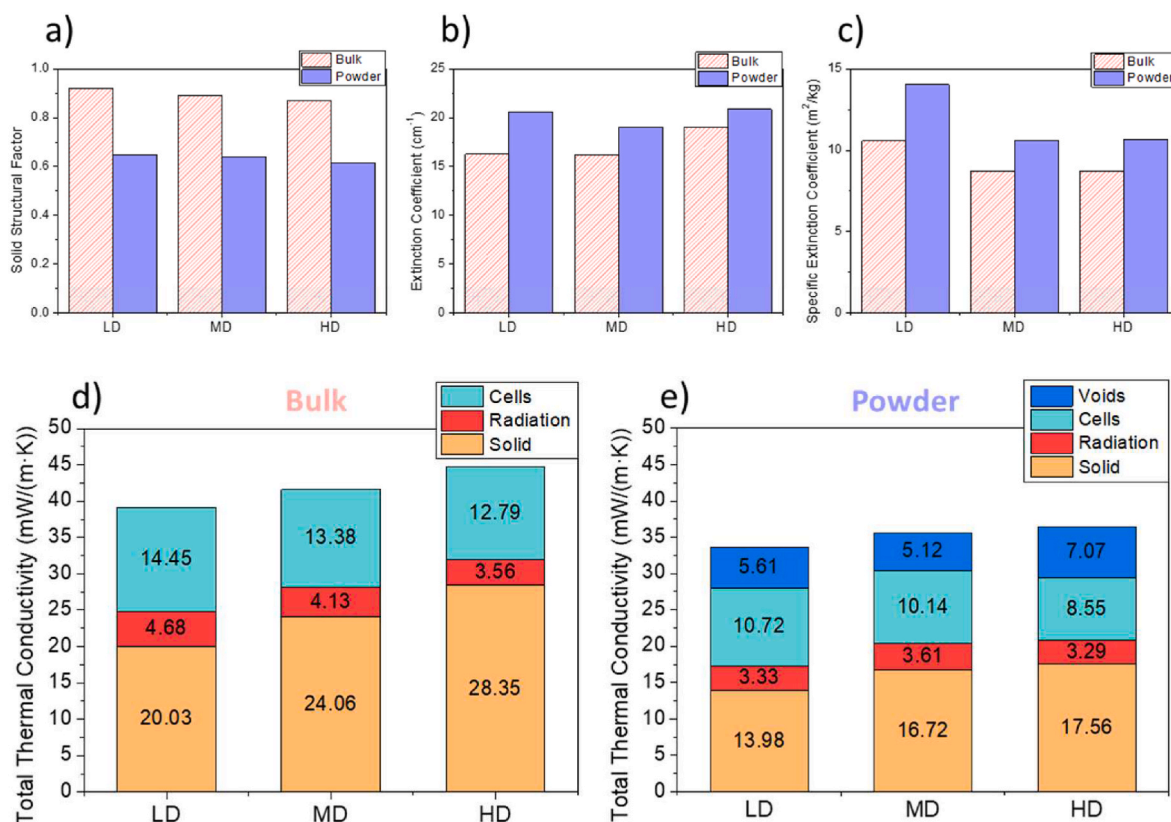
Fig. 8. Results of the study of the heat transfer mechanisms in the micronized nanocellular samples: a) solid structural factor and b) extinction coefficient calculated from the experimental results, c) specific extinction coefficient. Solid structural factors and extinction coefficients of the bulk samples have been included for sake of comparison. Contribution of each transfer mechanism to the total thermal conductivity at 10 °C of d) the bulk samples and e) the micronized nanocellular samples.

Rayleigh when the cell size is reduced, meaning that there is a stronger dependency on the wavelength in the scattering process and that the fraction of scattered radiation is sharply reduced [16,17]. Therefore, in nanocellular polymers, the extinction of radiation is mainly due to absorption when the cell size is on the nanometric scale [16]. In our previous work, the radiation was modeled as a function of the relative density and cell size of microcellular and nanocellular PMMA [17]. It was observed that the radiation contribution increases when the density and cell size are reduced [17]. In the powder materials, where density is reduced, one could expect a lower extinction coefficient since the fraction of solid to absorb radiation is lower. However, this is not the case: the extinction coefficient is always higher (Fig. 8b) and when the density is factor out the effect is even greater (Fig. 8c). Then, the reason for the higher extinction coefficient in the micronized samples (which present lower densities than the bulks samples but similar cellular structure) should be related to the presence of additional solid-gas interfaces that scatter radiation. Then, after micronization, the presence of micrometric voids increases the scattering of radiation and this effect dominates over the lack of radiation absorption in low-density samples (Fig. 8b). Finally, in Fig. 8d and 8e the contributions of each transfer mechanism (solid, cells, voids, and radiation) to the total thermal conductivity at 10 °C are presented. Note that the solid plus radiation contribution is reduced after the micronization process, revealing that this strategy is promising for enhancing the behavior of nanocellular polymers, especially for low-density materials.

Finally, regarding the contribution of the gas phase (cells and voids), it slightly increases (Fig. 8d and 8e) due to the lower density and the presence of air between the powder particles. However, this increase of about 2 mW/(m·K) is offset by the reductions in the other two mechanisms which are higher than 8 mW/(m·K).

All these calculations help to understand that density reduction is not
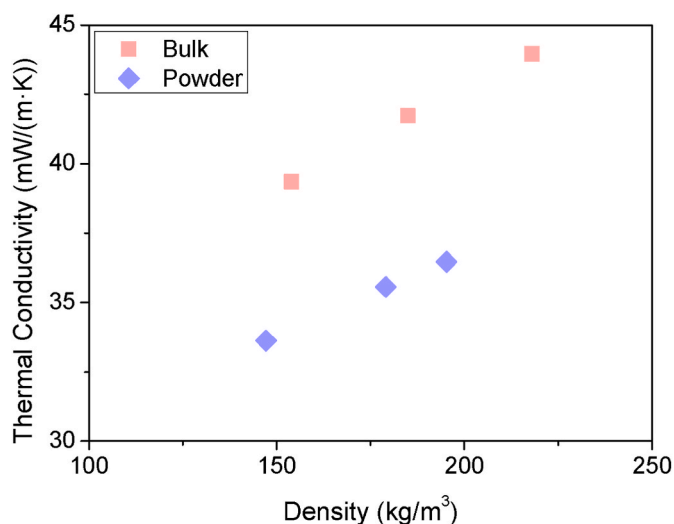

Fig. 9. Thermal conductivity measured at 10 °C as function of the material apparent density of the bulk and micronized LD, MD and HD samples.

the main responsible of the reduced density of the micronized material: solid phase discontinuity and radiation scattering are the main factors. In fact, the HD powder (with apparent density 194 kg/m³) presents lower thermal conductivity (36.5 vs. 39.3 mW/(m·K)) than the LD bulk sample, which presents a much lower density (154 kg/m³) (Fig. 7). Then, the powder can be a better thermal insulator than the bulk material even with a higher density (Fig. 9).

5. Conclusions

In this work, three nanocellular PMMA powders with different densities and the same cell size (around 400 nm) have been produced and characterized. After micronization, the density is reduced (around 10%) due to the presence of voids between the powder particles, reaching apparent densities in the range of 130–190 kg/m^3. The powder packing has been analyzed by X-ray tomography. Results show that the powder particles suffer an increase in density during the micronization process of around 22% in comparison with the bulk material. However, the cellular structure is preserved. Furthermore, the micronization process helps to interconnect the cellular structure, leading to an open cell content rise (higher than 90%). In addition, particle size distribution has been studied with dynamic laser diffraction, image analysis, and X-ray tomography obtaining similar trends despite the differences between the techniques. The void size was also calculated through X-ray tomography leading to a value of around 20 μm.

Finally, the thermal conductivity of the powder materials was measured. Results prove that the micronization process leads to a reduction of thermal conductivity. However, this reduction is not only due a density reduction, but a change in the heat transfer mechanisms. The analysis shows that the solid structural factor decreases about 29% after micronization probably due to the transition from a continuous cellular structure (bulk sample) to a discontinuous structure (powder material) where the contact points between the powder particles act as additional thermal resistances. As a consequence, the contribution of the solid phase to the conduction process is reduced in the micronized materials due to their lower density and their reduced structural factor. Furthermore, the presence of micrometric voids increases the radiation scattering, leading to a higher extinction coefficient and reduced thermal radiation in comparison with the bulk samples. The obtained results are promising since the micronized nanocellular polymers seem to offer a solution to boost the performance of nanocellular polymers, paving the way to improve forward their thermal insulation behavior.

CRediT authorship contribution statement

Ismael Sánchez-Calderón: Conceptualization, Methodology, Investigation, Formal analysis, Writing – original draft. **Victoria Bernardo:** Conceptualization, Investigation, Supervision, Writing - Review. **Daniel Cuadra-Rodríguez:** Investigation, Writing - Review. **Judith Martín-de-León:** Conceptualization, Supervision, Writing - Review. **Miguel Ángel Rodríguez-Pérez:** Conceptualization, Supervision, Writing - Review, Funding acquisition.

Declaration of competing interest

The authors declare that they have no known competing financial interests or personal relationships that could have appeared to influence the work reported in this paper.

Data availability

Data will be made available on request.

Acknowledgments

Appendix A. Supplementary data

Supplementary data to this article can be found online at https://doi.org/10.1016/j.polymer.2022.125397.

References

[1] B. Xiang, Z. Deng, F. Zhang, N. Wen, Y. Lei, T. Liu, S. Luo, Microcellular silicone rubber foams: the influence of reinforcing agent on cellular morphology and nucleation, Polym. Eng. Sci. 59 (2019) 5–14, https://doi.org/10.1002/pen.24857.

[2] J. Martín-de León, V. Bernardo, M.Á. Rodríguez-Pérez, Key production parameters to obtain transparent nanocellular PMMA, Macromol. Mater. Eng. 302 (2017), 1700343, https://doi.org/10.1002/mame.201700343.

[3] G.Q. Lu, X.S. Zhao, Nanoporous materials - an overview, in: Nanoporous Mater. Sci. Eng., Imperial College Press, 2004, pp. 1–13, https://doi.org/10.1142/9781860946561_0001.

[4] B. Notario, J. Pinto, R. Verdejo, M.A. Rodríguez-Pérez, Dielectric behavior of porous PMMA: from the micrometer to the nanometer scale, Polymer 107 (2016) 302–305, https://doi.org/10.1016/j.polymer.2016.11.030.

[5] B. Notario, A. Ballesteros, J. Pinto, M.A. Rodríguez-Pérez, P.M.M.A. Nanoporous, A novel system with different acoustic properties, Mater. Lett. 168 (2016) 76–79, https://doi.org/10.1016/j.matlet.2016.01.037.

[6] B. Notario, J. Pinto, E. Solorzano, J.A. de Saja, M. Dumon, M.A. Rodríguez-Pérez, Experimental validation of the Knudsen effect in nanocellular polymeric foams, Polymer 56 (2015) 57–67, https://doi.org/10.1016/j.polymer.2014.10.006.

[7] S.A. Mofid, B.P. Jelle, X. Zhao, T. Gao, M. Grandcolas, B. Cunningham, S. Ng, R. Yang, Utilization of size-tunable hollow silica nanospheres for building thermal insulation applications, J. Build. Eng. 31 (2020), 101336, https://doi.org/10.1016/j.jobe.2020.101336.

[8] H. Ebert, Thermal properties of aerogels, in: Aerogels Handb, 2011, pp. 537–564, https://doi.org/10.1007/978-1-4419-7589-8.

[9] Z.-Y. Li, C.-Y. Zhu, X.-P. Zhao, A theoretical and numerical study on the gas-contributed thermal conductivity in aerogel, Int. J. Heat Mass Tran. 108 (2017), https://doi.org/10.1016/j.ijheatmasstransfer.2017.01.051, 1982–1990.

[10] H. Singh, M. Geisler, F. Menzel, Experimental investigations into thermal transport phenomena in vacuum insulation panels (VIPs) using fumed silica cores, Energy Build. 107 (2015) 76–83, https://doi.org/10.1016/j.enbuild.2015.08.004.

[11] S. Costeux, CO2-Blown nanocellular foams, J. Appl. Polym. Sci. 131 (2014), https://doi.org/10.1002/app.41293.

[12] S. Liu, J. Duvigneau, G.J. Vancso, Nanocellular polymer foams as promising high performance thermal insulation materials, Eur. Polym. J. 65 (2015) 33–45, https://doi.org/10.1016/j.eurpolymj.2015.01.039.

[13] C. Forest, P. Chaumont, P. Cassagnau, B. Swoboda, P. Sonntag, Polymer nano-foams for insulating applications prepared from CO2 foaming, Prog. Polym. Sci. 41 (2015) 122–145, https://doi.org/10.1016/j.progpolymsci.2014.07.001.

[14] G. Wang, C. Wang, J. Zhao, G. Wang, C.B. Park, G. Zhao, Modelling of thermal transport through a nanocellular polymer foam: toward the generation of a new superinsulating material, Nanoscale 9 (2017) 5996–6009, https://doi.org/10.1039/c7nr00327g.

[15] P. Buahom, C. Wang, M. Alshrah, G. Wang, P. Gong, M. Tran, C.B. Park, Wrong expectation of superinsulation behavior from largely-expanded nanocellular foams, Nanoscale (2020), https://doi.org/10.1039/d0nr01927e.

[16] V. Bernardo, J. Martin-de Leon, J. Pinto, U. Schade, M.A. Rodriguez-Perez, On the interaction of infrared radiation and nanocellular polymers: first experimental determination of the extinction coefficient, Colloids Surfaces A Physicochem. Eng. Asp. 600 (2020), https://doi.org/10.1016/j.colsurfa.2020.124937.

[17] I. Sánchez-Calderón, V. Bernardo, J. Martín-de-León, M.Á. Rodríguez-Pérez, Thermal conductivity of low-density micro- and nanocellular poly(methyl-methacrylate) (PMMA): experimental and modeling, Mater. Des. 221 (2022), 110938, https://doi.org/10.1016/j.matdes.2022.110938.

[18] P. Buahom, P. Gong, C. Wang, H. Yu, J. Liu, C.B. Park, Carbon as a solution for nanocellular foam superinsulation, Carbon N. Y. 189 (2022) 319–338, https://doi.org/10.1016/j.carbon.2021.11.041.

[19] F. Almeida, H. Beyrichen, N. Dodamani, R. Caps, A. Muller, R. Oberhoffer, Thermal Conductivity Analysis of a New Sub-micron Sized Polystyrene Foam, 2020, https://doi.org/10.1177/0021955X20943101.

[20] Y. Li, Z. Chen, C. Zeng, Poly(Methyl methacrylate) (PMMA) nanocomposite foams, in: Polym. Nanocomposite Foam, 2018.

[21] V. Bernardo, J. Martin de Leon, J. Pinto, R. Verdejo, M.A. Rodriguez-Perez, Modeling the heat transfer by conduction of nanocellular polymers with bimodal cellular structures, Polymer 160 (2019) 126–137, https://doi.org/10.1016/j.polymer.2018.11.047.

[22] P. Gong, G. Wang, M.P. Tran, P. Buahom, S. Zhai, G. Li, C.B. Park, Advanced bimodal polystyrene/multi-walled carbon nanotube nanocomposite foams for thermal insulation, Carbon N. Y. 120 (2017) 1–10, https://doi.org/10.1016/j.carbon.2017.05.029.

[23] N.M. Demewoz, S.K. Yeh, Fabrication and characterization of low-density nanocellular foam based on PMMA/TPU blends, Polymer 240 (2022), 124493, https://doi.org/10.1016/j.polymer.2021.124493.

[24] S. Yeh, N.M. Demewoz, V. Kurniawan, Controlling the structure and density of PMMA bimodal nanocellular foam by blending different molecular weights, Polym. Test. (2020), https://doi.org/10.1016/j.polymertesting.2020.107004.

[25] M. Reim, W. Körner, J. Manara, S. Korder, M. Arduini-Schuster, H.P. Ebert, J. Fricke, Silica aerogel granulate material for thermal insulation and daylighting, Sol. Energy 79 (2005) 131–139, https://doi.org/10.1016/j.solener.2004.08.032.

[26] X. Lu, R. Caps, J. Fricke, C.T. Alviso, R.W. Pekala, Correlation between structure and thermal conductivity of organic aerogels, J. Non-Cryst. Solids 188 (1995) 226–234, https://doi.org/10.1016/0022-3093(95)00191-3.

[27] J. Fricke, Thermal Transport in Porous Superinsulations, 1986, pp. 94–103, https://doi.org/10.1007/978-3-642-93313-4_11.

[28] L.W. Hrubesh, R.W. Pekala, Thermal properties of organic and inorganic aerogels, J. Mater. Res. 9 (1994) 731–738, https://doi.org/10.1557/JMR.1994.0731.

[29] V. Napp, R. Caps, H. Ebert, Optimization of the thermal radiation extinction of silicon carbide in a silica powder matrix, J. Therm. Anal. Calorim. 56 (1999) 77–85, https://doi.org/10.1023/A:1010131324100.

[30] R. Caps, J. Fricke, Thermal conductivity of opacified powder filler materials for vacuum insulations, Int. J. Thermophys. 21 (2000) 445–452, https://doi.org/10.1023/A:1006691731253.

[31] M. Davraz, M. Koru, H.C. Bayrakçi, Y. Yusufoğlu, O. Ipek, The effect of opacifier properties on thermal conductivity of vacuum insulation panel with fumed silica, J. Therm. Anal. Calorim. 142 (2020) 1377–1386, https://doi.org/10.1007/s10973-020-09277-8.

[32] ISO 60:1997 Plastics — Determination of Apparent Density of Material that Can Be Poured from a Specified Funnel, 1997.

[33] E. Solórzano, J. Pinto, S. Pardo, F. Garcia-Moreno, M.A. Rodriguez-Perez, Application of a microfocus X-ray imaging apparatus to the study of cellular polymers, Polym. Test. 32 (2013) 321–329, https://doi.org/10.1016/j.polymertesting.2012.11.016.

[34] A. Ballesteros, E. Laguna-Gutierrez, P. Cimavilla-Roman, M.L. Puertas, A. Esteban-Cubillo, J. Santaren, M.A. Rodriguez-Perez, Influence of the dispersion of Nanoclays on the cellular structure of foams based on polystyrene, J. Appl. Polym. Sci. 138 (2021) 1–19, https://doi.org/10.1002/app.51373.

[35] P. Cimavilla-Román, S. Pérez-Tamarit, S. Barroso-Solares, J. Pinto, M.Á. Rodríguez-Pérez, Sub-pixel tomographic methods for characterizing the solid architecture of foams, Microsc. Microanal. (2022) 1–12, https://doi.org/10.1017/s1431927622000447.

[36] M. Dierick, B. Masschaele, L. Van Hoorebeke, Octopus, a fast and user-friendly tomographic reconstruction package developed in LabView, Meas. Sci. Technol. 15 (2004) 1366–1370, https://doi.org/10.1088/0957-0233/15/7/020.

[37] A. Rawle, Basic of principles of particle size analysis, Surf. Coating. Int. Part A, Coatings J. (2003). https://www.atascientific.com.au/basic-principles-of-particle-size-analysis/%0Ahttps://www.atascientific.com.au/.

[38] (n.d.), http://www.cellmattechnologies.com/en/software-and-methodology-for-the-characterization- of-cellular-structures/.

[39] ISO 9276-2:2014 Representation of Results of Particle Size Analysis — Part 2: Calculation of Average Particle Sizes/Diameters and Moments from Particle Size Distributions, 2014.

[40] ASTM C518 Standard Test Method for Steady-State, Thermal Transmission Properties by Means of the Heat Flow Meter Apparatus, 2017.

[41] ISO 8301 Thermal Insulation - Determination of Steady-State Thermal Resistance and Related Properties - Heat Flow Meter, 1991.

[42] N.C. Hilyard, A. Cunningham, Low Density Cellular Plastics Physical Basis of Behaviour, 1994, https://doi.org/10.1007/978-94-011-1256-7.

[43] Y.A. Cengel, A.J. Ghajar, Heat and Mass Transfer: Fundamentals & Applications Appendix 1, Fifth Edit, Mc Graw Hill Education, 2006.

[44] X. Chateau, Particle packing and the rheology of concrete, in: Underst. Rheol. Concr., Elsevier, 2012, pp. 117–143, https://doi.org/10.1533/9780857095282.2.117.

[45] A. Averardi, C. Cola, S.E. Zeltmann, N. Gupta, Effect of particle size distribution on the packing of powder beds: a critical discussion relevant to additive manufacturing, Mater. Today Commun. 24 (2020), 100964, https://doi.org/10.1016/j.mtcomm.2020.100964.